

Direct numerical simulation of turbulent flow over spanwise-varying roughness

M. X. Xie, A. Rouhi, D. Chung and N. Hutchins

Department of Mechanical Engineering, The University of Melbourne, VIC 3010, Australia

Abstract

We report direct numerical simulations (DNS) of turbulent flow through an open channel over spanwise-alternating patches of smooth and rough surfaces. The width of the patches is varied from $s/h \approx 0.40$ to $s/h \approx 12.72$, where h is the height of the channel. The roughness elements are fully resolved; here, they are three-dimensional sinusoids with fixed height $k/h = 0.056$ and fixed wavelength $\lambda = 7.1k$. The friction Reynolds number based on the global wall shear stress is 590. As the patch width increases, we find that the skin-friction coefficient decreases and the contrast between the rough and smooth wall shear stresses decreases. An intermediate patch size $s/h \approx 3.18$ is identified that separates the cases with significant spanwise heterogeneity from those near the homogeneous limit.

Introduction

Extensive research has been conducted over the past century to understand how surface roughness affects turbulent flow. Skin friction on ships and heat distribution in atmospheric boundary layers are just two of many important applications. Though significant advances have been made in our understanding of flow over spatially homogeneous roughness, rough surfaces in applications are often spatially heterogeneous. While the direction of heterogeneity depends on application, here we investigate the idealised configuration of spanwise-varying roughness, where the rough walls are homogeneous in the streamwise direction. Past studies of this configuration initially focused on secondary flows, where large-scale counter-rotating mean streamwise vorticity in the streamwise-normal plane arise from local production-to-dissipation imbalances of turbulent kinetic energy [1, 6]. More recently, studies investigated the effect of changing the spanwise spacing of roughness heterogeneity [4, 8, 12, 13]. Though spanwise-varying roughness has already been studied experimentally [8, 12] and computationally [4, 13], resolved flow data down to the roughness elements are still lacking, precluding direct investigation of the link between the aforementioned secondary motions and the wall shear stress. On the one hand, experiments have been subject to resolution limitations near the wall, especially for local measurements of wall shear stress; on the other hand, simulations have been subject to modelling assumptions that parametrise the effect of roughness elements on the near-wall flow. This study overcomes these limitations by using direct numerical simulation (DNS) that fully resolves the flow down to the wall, including the roughness elements. As a result, the wall shear stress distribution is directly quantified.

Flow Setup and Numerical Method

Let $\{x_1, x_2, x_3\} \equiv \{x, y, z\}$ denote the streamwise, spanwise and wall-normal coordinates, respectively, with $\{u_1, u_2, u_3\} \equiv \{u, v, w\}$ the corresponding velocities. The simulation is governed by the Navier–Stokes equations:

$$\frac{\partial u_i}{\partial x_i} = 0; \quad \frac{\partial u_i}{\partial t} + \frac{\partial u_i u_j}{\partial x_j} = -\frac{1}{\rho} \frac{\partial p}{\partial x_i} + \nu \frac{\partial^2 u_i}{\partial x_j \partial x_j} + \Pi \delta_{1i} + f_i. \quad (1)$$

Here, ρ is the density, p the pressure, ν the kinematic viscosity, $\Pi > 0$ the driving pressure gradient and f_i the direct forcing of

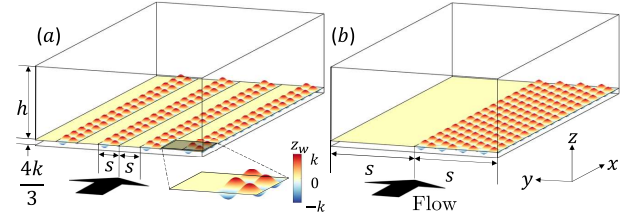


Figure 1: The computational domain is an open channel tiled with streamwise-aligned rough and smooth walls with varying patch widths: (a) $s/h \approx 0.40$ and (b) $s/h \approx 1.59$. The inset shows that the z -coordinate origin is defined relative to the smooth wall and that the rough wall varies between $\pm k$ in height, where $k = 0.056h$ is the semi-amplitude of the sinusoidal roughness.

the immersed-boundary method such that the volume-of-fluid interpolation of u_i is zero inside a solid cell [5, 10].

Figure 1 presents a schematic of the computational domain, which is an open channel whose bottom wall is characterised by spanwise-alternating patches of smooth and rough surfaces that are streamwise homogeneous. The width of both smooth and rough patches are equal to s , which is the parameter of interest in this paper. The rough walls are tiled by ‘egg-cartons’ described by $z_w = k \sin(2\pi x/\lambda) \sin(2\pi y/\lambda)$ [2]. Here, z_w is the local height of the bottom wall, $k = 0.056h$ the roughness height and $\lambda = 7.1k$ the roughness wavelength. $z = 0$ is defined at the smooth wall, which is $(4/3)k$ above the bottom of the computational domain and is aligned to the mean height of the rough patches. The streamwise and spanwise grid spacing is uniform, while the wall-normal computational grid spacing is uniform for $z \leq k$, i.e. below the roughness crest, and is stretched using a hyperbolic tangent mapping up to $z = h$. As detailed in table 1, the domain length is fixed at $L_x \approx 6.36h$ to accommodate an integer number of roughness wavelengths while ensuring it is large enough to capture accurate one-point statistics [7]. For the same reason, the width is $L_y \approx 3.18h$ for the simulations with $s/h \lesssim 1.59$. For the simulations where $s/h \gtrsim 3.18$, the domain width is $L_y = 2s$ so that it can fully contain one smooth patch and one rough patch. The stress-free ($\partial u/\partial z = \partial v/\partial z = 0$) and impermeable ($w = 0$) boundary conditions are imposed at the top surface ($z = h$). Periodic boundary conditions are imposed in the streamwise (x) and spanwise (y) directions.

The global friction Reynolds number of the flow $Re_{\tau_0} \equiv hu_{\tau_0}/\nu = 590$, where the friction velocity $u_{\tau_0} \equiv \sqrt{\tau_0/\rho}$. Here, τ_0 is the average wall shear stress and hence satisfies the relation $\tau_0 = h\Pi$.

The spatial and temporal discretisation schemes of the governing equations are detailed in [3]. Briefly, the governing equations are spatially discretised on a staggered grid using a fourth-order finite-difference scheme that conserves mass, momentum and energy. Time marching is achieved using a low-storage third-order Runge–Kutta scheme, in which the fractional-step method is applied at each sub-step to ensure a divergence-free velocity field.

Case	Marker	s/h	L_x/h	L_y/h	n_x	n_y	N_x	N_y	N_z	$\Delta_{x,R}^+$	$\Delta_{y,R}^+$	$\Delta_{z,R}^+$	Tu_{τ_0}/h
HS		Homogeneous smooth	6.28	3.14			384	384	318	9.77	4.89	0.34–6.93	10
HR		Homogeneous rough	6.36	3.18	24	48	384	384	400	9.77	4.89	0.35–6.98	10
S1	∇	0.40	6.36	3.18	16	32	256	256	200	17.42	8.71	0.83–16.58	10
S2	\triangle	0.80	6.36	3.18	16	32	256	256	200	17.86	8.93	0.85–16.99	10
S4	\square	1.59	6.36	3.18	16	32	256	256	200	17.64	8.82	0.84–16.78	10
S8	\star	3.18	6.36	6.36	16	32	256	512	200	17.10	8.55	0.82–16.27	10
S16	\diamond	6.36	6.36	12.72	6	12	96	384	100	42.26	21.13	1.08–58.84	12
S32	\circ	12.72	6.36	25.45	6	12	96	768	100	40.82	20.41	1.05–56.84	15

Table 1: Simulation cases at $Re_{\tau_0} = 590$. Spanwise-varying cases are identified by the letter ‘S’ followed by the number of sinusoids in the width of each rough patch. n_x and n_y are the number of grid points per sinusoid in the streamwise and spanwise directions, respectively. N_x , N_y and N_z are the number of grid points in the streamwise, spanwise and wall-normal directions, respectively. $\Delta_{x,R}^+$, $\Delta_{y,R}^+$ and $\Delta_{z,R}^+$ are the corresponding grid spacings scaled by $\nu/\sqrt{\tau_R/\rho}$, where τ_R is the average wall shear stress at the rough walls except for case HS, where τ_R is just the average wall shear stress. Tu_{τ_0}/h is the normalised duration over which statistics are collected after simulation transients are discarded.

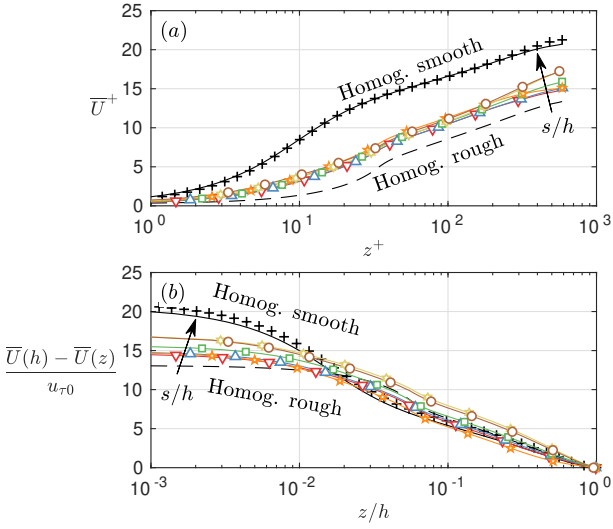


Figure 2: Profiles of (a) the mean velocity and (b) the mean velocity defect. Legend is consistent with table 1. ‘+’ full channel profile at matched Re_{τ_0} [9].

All statistics are ensemble averaged over duration T detailed in table 1. Quantities averaged in the streamwise direction are denoted using uppercase letters, as in $U(y, z) \equiv \langle u \rangle_x$, where the subscript x_i indicates averaging in the x_i direction. The mean streamwise velocity profile is denoted $\bar{U}(z) \equiv \langle U \rangle_y = \langle u \rangle_{xy}$. Note that averaged quantities are superficially averaged; that is, they are averages taken by zeroing the velocity in the solid.

Results and Discussion

Mean Quantities

The mean velocity profiles are presented in figure 2a, where $U^+ \equiv U/u_{\tau_0}$ and $z^+ \equiv z u_{\tau_0}/\nu$. We observe that the heterogeneous roughness cases ($s/h \gtrsim 0.40$) group close together but do not entirely collapse between the homogeneous smooth (HS) and homogeneous rough (HR) cases with matched Re_{τ_0} . The velocity defect profiles in figure 2b shows outer-layer collapse for $s/h \lesssim 3.18$. For $s/h \gtrsim 6.36$, where s is almost an order of magnitude larger than h , outer-layer similarity does not hold.

Integrating the momentum equation in (1) for $i = 1$ relates the

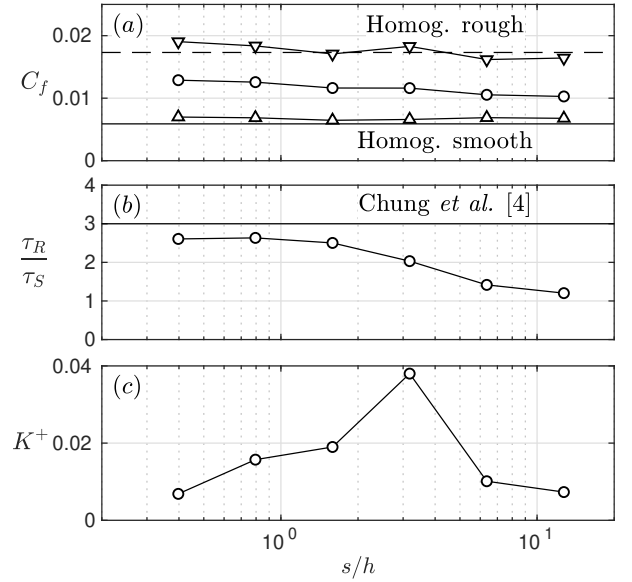


Figure 3: Effect of patch width s/h on: (a) C_f (\circ), the skin-friction coefficient, and $C_{f,R}$ (∇) and $C_{f,S}$ (\triangle) defined in (4); (b) τ_R/τ_S , the ratio of the rough and smooth wall shear stresses each averaged over their respective patches; and (c) $K^+ \equiv K/u_{\tau_0}^2$, where K , the average kinetic energy of the secondary motion is defined in (6).

average wall shear stress τ_0 to the immersed boundary force f_1 .

$$\tau_0 \equiv \frac{\rho}{L_x L_y} \int_0^{L_y} \int_0^{L_x} \left(\int_{-(4/3)k}^h f_1 dz \right) dx dy = h\Pi \quad (2)$$

The skin-friction coefficient is given by $C_f \equiv \tau_0/(\rho U_b^2/2)$, where $U_b \equiv \langle \bar{U} \rangle_z$. C_f is plotted in figure 3a, from which we observe that it reduces as patch size s/h increases.

Wall Shear Stress Distribution

In the presence of surface heterogeneity, the wall shear stress distribution depends greatly on the surface geometry. We define τ_R and τ_S as the streamwise wall shear stresses averaged over the rough walls (R) and over the smooth walls (S), respectively.

$$\tau_{R,S} \equiv \frac{\rho}{L_x(L_y/2)} \int_{y \in R,S} \int_0^{L_x} \left(\int_{-(4/3)k}^h f_1 dz \right) dx dy \quad (3)$$

We can subsequently define the skin friction coefficient over the smooth and rough walls as

$$C_{f,R,S} \equiv \frac{\tau_{R,S}}{\rho U_{b,R,S}^2/2}, \quad \text{where } U_{b,R,S} \equiv \int_{y \in R,S} \langle u \rangle_{x,z} dy. \quad (4)$$

Despite the ratio τ_R/τ_S changing greatly with s/h in figure 3b, figure 3a shows that $C_{f,R}$ and $C_{f,S}$ are remarkably close to C_f for the homogeneous rough and homogeneous smooth cases, respectively. The underlying mechanism causing this behaviour remains unresolved.

Figure 3b shows that τ_R/τ_S decreases and approaches unity for increasing s/h . A similar trend is observed in the open channel large-eddy simulations (LES) of [13], where the maximum wall shear stress over the higher roughness patch decreased as its width increased. $\tau_R/\tau_S = 1$ is the limiting case where both patches impose the same amount of drag to the fluid, and its tendency to unity for increasing s/h hints to the existence of a spanwise distance beyond which the wall shear stress can be effectively ‘transported’ across a change in surface roughness. Where the patch size is relatively small ($s/h \lesssim 3.18$), the flow over a patch is ‘fully aware’ of the neighbouring patches and will subsequently lead to a non-uniform distribution of wall shear stress. Contrast this with large patch size cases ($s/h \gtrsim 12.72$), where the computational domain is just the concatenation of two independent channels (one smooth and one rough) but with a small mixing region between them. As a result, the wall shear stress over each patch predominantly balances with the driving pressure gradient with little consideration of the flow over its neighbouring patches.

To further probe the distribution of wall shear stress, we calculate $\tilde{\tau}_x(y)$ and $\tilde{\tau}_y(y)$, the local streamwise and spanwise wall shear stresses, by integrating f_1 and f_2 , respectively.

$$\tilde{\tau}_{x,y}(y) = \frac{\rho}{L_x \lambda} \int_{y-\lambda/4}^{y+\lambda/4} \int_0^{L_x} \left(\int_{-(4/3)k}^h f_{1,2} dz \right) dx dy \quad (5)$$

The integration domain in (5) has width $\lambda/2$ corresponding to the width of a half-sinusoid. The spanwise distributions of $\tilde{\tau}_x$ and $\tilde{\tau}_y$ are shown in the left and right columns of figure 4, respectively. We observe that the magnitude of $\tilde{\tau}_y$ is about an order of magnitude lower than that of $\tilde{\tau}_x$, consistent with the open channel LES of [13] with friction Reynolds numbers orders of magnitude larger than the present simulations. Whereas the aforementioned LES [13] observed that the peaks in the spanwise wall shear stress occur within the rough patch, we observe that the peaks occur at the wall transitions $y/s = \pm 0.5$. One likely reason for this difference is the implementation of surface roughness. The roughness elements in the simulations presented herein are fully resolved with spanwise wavelength $\lambda \approx 0.40h$; contrariwise, the surface roughness in the LES of [13] is parameterised by the surface drag approximated via the equilibrium logarithmic law in the absence of a physical roughness geometry. Consequently, near-wall flow around the roughness elements will differ and lead to a different distribution of wall shear stress.

Secondary Motion

The average kinetic energy of the secondary motion K is defined as follows.

$$K \equiv \frac{1}{L_y h} \int_0^{L_y} \int_0^h \frac{1}{2} (V^2 + W^2) dy dz \quad (6)$$

K peaks at $s/h \approx 3.18$ (figure 3c), meaning the secondary motion is likely sustained via some mechanism. This is consistent with the analysis of Townsend [11, pp. 328–331], which

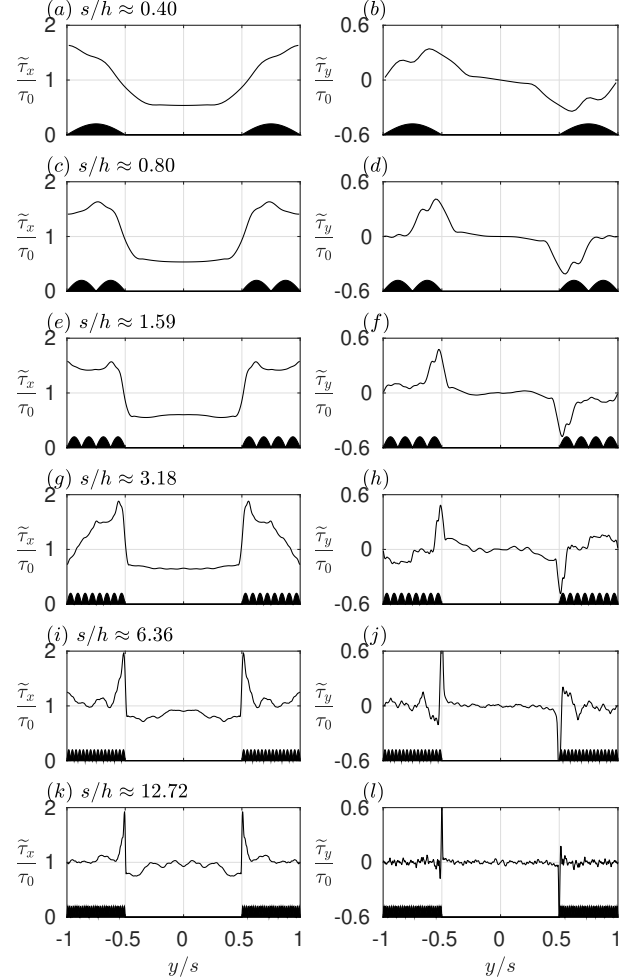


Figure 4: Spanwise distributions of: (left panels) the streamwise wall shear stress $\tilde{\tau}_x$; and (right panels) the spanwise wall shear stress $\tilde{\tau}_y$. y is scaled by s so that the spanwise extent of the cases are comparable. The smooth wall lies in the range $|y/s| < 0.5$.

predicted that secondary motions are sustained in tandem with spanwise variations of wall shear stress with characteristic wavelength of 4.2 boundary-layer thicknesses. In the present study, $s/h \approx 3.18$ corresponds to a characteristic wavelength of $6.36h$ for the wall shear stress. For $s/h \gtrsim 0.80$ (figures 5b–f), vortex pairs with size comparable to the channel height cover the domain. At $s/h \approx 3.18$ (figure 5d), not only do the vortices appear strongest, there is also a strong diagonal cross-flow at the roughness transition due to a small vertical offset between the vortex centre above the smooth wall and that over the rough wall. These observations hint that $s/h \approx 3.18$ is an intermediate patch size that separates the spatially heterogeneous cases ($s/h \gtrsim 6.36$) from the spatially homogeneous limit, consistent with the results of a similar study [4]. For large $s/h \gtrsim 6.36$ (figures 5e–f), vortices also appear in the centre of each patch away from the wall transitions, similar to the tertiary flows that are identified in the boundary layer experiments of [12] for large roughness spacing.

As discussed in similar studies [4, 12], the roughness patch size affects the mean flow, which is shown in figure 5. The $U(y, z)$ isovels for $s/h \lesssim 1.59$ (figures 5a–c) appear flat and exhibit little spanwise heterogeneity. Contrariwise, the isovels for $s/h \gtrsim 6.36$ (figures 5e–f) are globally heterogeneous, but are locally homogeneous above the centre of each patch. $s/h \approx 3.18$ (figure 5d) is the only patch size for which the flow shows nei-

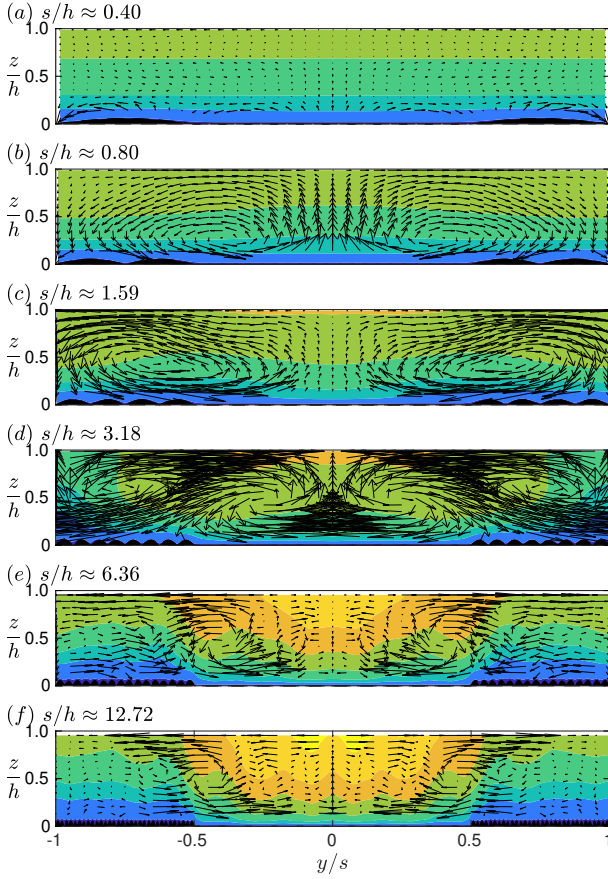


Figure 5: yz -plane cross section of the channel scaled by patch size s in the spanwise direction with mean streamwise contours (isovels) at $U/u_{\tau 0} = 5, 10, 12, 14, 16, 18, 20$. The in-plane secondary flow $[V, W]/u_{\tau 0}$ is indicated by the vector arrows, scaled equally across the panels.

ther the global homogeneity observed for $s/h \lesssim 1.59$ nor the local homogeneity observed for $s/h \gtrsim 6.36$, which is yet another indicator that it is an intermediate patch size between the two patch size regimes.

Conclusions

Flow over spanwise heterogeneous surfaces with different roughness patch size s/h is studied in this paper through DNS of an open channel at friction Reynolds number $Re_{\tau 0} = 590$. For the three smallest patch sizes where $s/h \lesssim 1.59$, we report little spanwise heterogeneity in the mean streamwise isovels despite the presence of in-plane vortices. For the two largest patch sizes $s/h \approx 6.36$ and $s/h \approx 12.72$, the primary flow directly above the centre of the smooth and rough patches appear locally homogeneous and mix only in a confined region around the roughness transition. The intermediate patch size $s/h \approx 3.18$ has the most energetic secondary motions and exhibits neither the aforementioned global homogeneity nor local homogeneity. $s/h \approx 3.18$ appears to separate the spatially heterogeneous cases ($s/h \gtrsim 6.36$) from the spatially homogeneous cases ($s/h \lesssim 1.59$). In terms of the wall shear stress distribution, the contrast between the rough and smooth walls (τ_R/τ_S) is as large as 2.63 for $s/h \approx 0.80$ and reduces towards unity as the patch size s/h increases. This limiting value represents the expected homogenisation of wall shear stress since both the smooth and rough patches are driven by the same pressure gradient. The skin-friction coefficient is also observed to decrease with patch size s/h .

Acknowledgements

This work was supported by resources provided by The Pawsey Supercomputing Centre with funding from the Australian Government and the Government of Western Australia and by the National Computational Infrastructure (NCI), which is supported by the Australian Government. This research was supported under the Australian Government Research Training Program Scholarship as well as the Australian Research Council's Discovery Project (DP160102279).

References

- [1] Anderson, W., Barros, J., Christensen, K. and Awasthi, A., Numerical and experimental study of mechanisms responsible for turbulent secondary flows in boundary layer flows over spanwise heterogeneous roughness, *J. Fluid Mech.*, **768**, 2015, 316–347.
- [2] Chan, L., MacDonald, M., Chung, D., Hutchins, N. and Ooi, A., A systematic investigation of roughness height and wavelength in turbulent pipe flow in the transitionally rough regime, *J. Fluid Mech.*, **771**, 2015, 743–777.
- [3] Chung, D., Chan, L., MacDonald, M., Hutchins, N. and Ooi, A., A fast direct numerical simulation method for characterising hydraulic roughness, *J. Fluid Mech.*, **773**, 2015, 418–431.
- [4] Chung, D., Monty, J. P. and Hutchins, N., Similarity and structure of wall turbulence with lateral wall shear stress variations, *J. Fluid Mech.*, **847**, 2018, 591–613.
- [5] Fadlun, E., Verzicco, R., Orlandi, P. and Mohd-Yusof, J., Combined immersed-boundary finite-difference methods for three-dimensional complex flow simulations, *J. Comput. Phys.*, **161**, 2000, 35–60.
- [6] Hinze, J., Secondary currents in wall turbulence, *Phys. Fluids*, **10**, 1967, S122–S125.
- [7] Lozano-Durán, A. and Jiménez, J., Effect of the computational domain on direct simulations of turbulent channels up to $re_{\tau} = 4200$, *Phys. Fluids*, **26**, 2014, 011702.
- [8] Medjnoun, T., Vanderwel, C. and Ganapathisubramani, B., Characteristics of turbulent boundary layers over smooth surfaces with spanwise heterogeneities, *J. Fluid Mech.*, **838**, 2018, 516–543.
- [9] Moser, R. D., Kim, J. and Mansour, N. N., Direct numerical simulation of turbulent channel flow up to $Re_{\tau} = 590$, *Phys. Fluids*, **11**, 1999, 943–945.
- [10] Scotti, A., Direct numerical simulation of turbulent channel flows with boundary roughened with virtual sandpaper, *Phys. Fluids*, **18**, 2006, 031701.
- [11] Townsend, A. A., *The Structure of Turbulent Shear Flow*, Cambridge University Press, 1976, Second edition.
- [12] Vanderwel, C. and Ganapathisubramani, B., Effects of spanwise spacing on large-scale secondary flows in rough-wall turbulent boundary layers, *J. Fluid Mech.*, **774**, 2015, R2.
- [13] Willingham, D., Anderson, W., Christensen, K. and Barros, J., Turbulent boundary layer flow over transverse aerodynamic roughness transitions: induced mixing and flow characterization, *Phys. Fluids*, **26**, 2014, 025111.